Unraveling Transfer Hydrogenation Mechanisms by Ammonia Borane to Alkenes over Self-Healing Copper Nanoparticles: The Complementary Role of N–H Bond, Surface, and Solvent

Unraveling Transfer Hydrogenation Mechanisms by Ammonia Borane to Alkenes Over Self-Healing Copper Nanoparticles: the Complementary Role of N-H Bond, Surface, and Solvent

Angelo Maspero,[a] *Fabrizio Bardelli,*[b] *Konstantis F. Konidaris,*[a] *Matteo Uboldi,*[a] *Carlo Lucarelli,*[a] *Nicola Schiaroli,*[a] *Jenny G. Vitillo*[a,*]

[a]Department of Science and High Technology and INSTM, Università degli Studi dell'Insubria, Via Valleggio 9, 22100 Como, Italy.

[b]Institute of Nanotechnology, National Research Council, Piazzale Aldo Moro, 5, 00185, Rome, Italy.

KEYWORDS. Copper, transfer hydrogenation, catalysts, ammonia borane, nanoparticles, density functional theory.

ABSTRACT. Ammonia borane-based transfer hydrogenation mechanisms on copper nanoparticles (CuNPs) are identified and assessed by isotope labeling and Kohn-Sham density functional methods, using the hydrogenation of styrene to ethylbenzene at ambient conditions as the model reaction. The key role of protonic solvents in permitting the ammonia borane decomposition is confirmed. Different dehydrogenation pathways are evidenced for the N–H and

B–H bonds: while the metal surface always acts as an intermediary in the hydrogen transfer from the B–H bond to the organic substrate, the N–H bond can directly hydrogenate the most negatively charged carbon atom of the unsaturated bond. The styrene to ethylbenzene reaction is here proved to have a > 99% conversion with 100% selectivity at ambient conditions, using methanol, and pure water as the solvents. The CuNPs are obtained *in situ* by reduction of the copper source, SION-X ($Cu_2[(BO)(OH)_2](OH)_3$), by ammonia borane. The catalytic properties of these CuNPs are stable for at least 5 cycles without the need for reduction steps, also upon their exposure to the air in between subsequent cycles. This is due to ammonia borane's ability to act simultaneously as the hydrogen source for the reaction and as the reducing agent of copper. Ammonia borane shows then a significant advantage to other hydrogen sources for transfer hydrogenation in combination with CuNPs, eliminating both the catalyst preparation and activation steps, reducing the complexity and operational cost of the process.

1. INTRODUCTION

Catalytic hydrogenations are an important class of reactions with many applications in several industrial sectors[1] such as food industry,[2, 3] petrochemicals,[4] pharmaceuticals,[5] material science,[6] and energy production.[7] Hydrogenation of olefins and aromatics towards their saturated derivatives is often at the core of chemical industrial processes to increase the commercial values of different chemical products.[8-10] These processes are generally carried out at high temperatures and, depending on the application, can be performed in the gas or liquid phase using pressurized H_2. Noble metal-based catalysts, such as Pd/C and Pt/Al_2O_3,[11, 12] display high selectivity and conversion rate but at the expense of high cost and low sustainability. First row transition metal-based catalysts (e.g. Raney nickel) often require harsher reaction conditions than their noble metal

counterparts and are more prone to deactivation, increasing the energy demand of the processes.[13-15] Among heterogeneous catalysts, metal nanoparticles (NPs) and clusters possess unique catalytic properties due to their size.[16] They can play a central role in solving stability and activity issues typical of first row transition metal-based catalysts, while still requiring close to ambient reaction conditions, a key factor for keeping low the cost of the process.[17] Scharnagl et al.[18] reported a biowaste-derived cobalt chitosan catalysts obtained through pyrolysis (at 700 °C) active in the hydrogenation of styrene (conversion 96%) and 1-octene (conversion 100%) at 60 °C and 10 bar of H_2 for 18 h. A nickel silicide/SiO_2 nano-catalyst obtained by thermal treatment (1000 °C, 2 h) was found to be highly active for the hydrogenations of very different organic substrates (nitroarenes, aldehydes, ketones, and alkenes among others) at 10-50 bar of H_2 and temperatures of 40-100 °C.[19] Zhang et al.[20] have recently reported the efficient hydrogenation at 30-200 °C and 1-40 bar of H_2 of different olefins and aromatics over highly dispersed Ni^0 nanoparticles anchored on a MCM-41 support. Nevertheless, the formation and (re)activation of the catalytic centers in all these systems need high temperatures and an H_2 stream.

The transfer hydrogenation of organic compounds is a safer process than reduction reactions involving pressurized molecular hydrogen.[21, 22] Transfer hydrogenation lies on the use of hydrogen-rich materials (in liquid or solid form) that, undergoing dehydrogenation, act as on-site hydrogen source.[23, 24] Ammonia borane (NH_3BH_3, AB) is a well-known water soluble, non-toxic, and air-stable source of H_2 that in the presence of a catalyst can release H_2 in the reaction environment at ambient conditions.[25] For these reasons, AB is among the most studied hydrogen source for transfer hydrogenation reactions.[26-31] AB dehydrogenation can be achieved through solvolysis in a protic solvent (often water – hydrolysis – or methanol – methanolysis) and it is catalyzed over a wide range of catalysts,[32, 33] such as noble metals NPs (Pt, Au, Rh, Ru, and Pd)[34]

and transition metals NPs, such as Ni, Fe, Cu and Co.[35-37] Among the latter, Cu(0) nanoparticles (CuNPs) present several advantages as hydrogenation catalysts, like high conversion rates and low cost.[38-40] Additionally, copper has the peculiarity to have a negative standard oxidation potential. This makes the catalysts based on Cu^0, although still air sensitive,[41] less prone to be oxidized, and then requiring less frequent reactivation cycles, with respect to the other first-row transition metals NPs.

Recent works have reported the quantitative semi-hydrogenation of different alkynes at 40-60 °C and atmospheric pressure using AB and $CuCl_2$,[42] or $CuSO_4$,[43] as precursors for *in situ* generation of CuNPs. Du et al.[44] demonstrated that a commercially available CuO powder can be also reduced by AB to generate a spongy structure consisting of CuNPs highly active in the hydrogenation of nitroarenes at 50 °C.

An additional problem of heterogeneous metal-based catalysts (noble or non-noble ones) is the fact that the metal nanoparticles tend to aggregate, causing a change in their activity in time.[41, 45] The main strategies for the stabilization of CuNPs involve the use of capping agents,[41, 46] alloying with other metals,[47] the formation of core-shell structures,[48] and the distribution of the nanoparticles over supports of very different composition.[49, 50] Yu et al.[50] studied the activity of CuNi NPs assembled over graphene, in the tandem hydrogenation of aromatic nitro compounds to primary amines using AB, reporting high conversions (>97%) and good stability at ambient temperature and pressure. Nanoporous core-shell Cu/Cu_2O NPs ($Cu@Cu_2O$) obtained from the dealloying of a CuAl precursor were found to be highly active and stable over 5 reaction cycle in the reduction of nitroarenes with AB.[51] Metal-organic frameworks-supported Cu nanoparticles have been reported to catalyze selectively the transfer hydrogenation of quinolines by AB at ambient conditions.[52] Nevertheless, all these strategies complicate the synthetic protocol, without

eliminating the problem related to the oxidation of the nanoparticles. Moreover, the additive deters the aggregation of the particles, but it alters (if not even poisons) the catalyst. Homogeneous catalysts are less affected by aggregation problems, although they cannot be easily separated by the products.

Different studies[42-44, 53, 54] have recently highlighted that issues related to oxidation are intrinsically minimized for CuNPs by the use of AB as the hydrogen source. AB serves in fact at the same time for the hydrogenation reaction and the reduction of the copper source to Cu(0) species, so forming *in situ* the CuNPs in the reaction environment and maintaining them in the reduced state, minimizing the need of reactivation. Oxidized copper species formed by contact with the air are also reduced by AB. This eliminates the need for the catalyst preparation and regeneration (calcination/oxidation, reduction, or surface cleaning). Moreover, the AB solvolysis products, can be converted back to AB or to boric acid:[42, 55-57] e.g., $NH_4B(OCH_3)_4$, can be regenerated to AB upon reaction with $LiAlH_4$ and NH_4Cl under ambient conditions.[58] The separation of the catalyst from the solution is often complicated for unsupported nanoparticles. Moreover, safety issues are often raised for the handling of dried unsupported NPs.[59] Kinik et al.[53, 54] reported the use of a self-healing catalyst named Jacquesdietrichite[60] or SION-X (formula: $Cu_2[(BO)(OH)_2](OH)_3$, see Figure 1a and Figure S1), that can serve as copper source for CuNPs and it is able to affect the selective transfer hydrogenation of nitroarenes by AB at ambient conditions. Interestingly, AB is selectively decomposed by SION-X to H_2, without borane formation.[53, 54] Unlike other copper sources, this mineral can be reformed quantitatively after the transfer hydrogenation reaction, by exposure of the solution to the air. The mechanism behind the self-healing properties of these CuNPs is discussed in Refs. 53, 54. Being SION-X solubility in water negligible, it can be then filtrated out from the solution at the end of the reaction or simply

reused for multiple times without significant catalyst deactivation.[44, 45] However, despite the great potential of CuNPs synthetized from SION-X as hydrogenation catalyst, they have not been tested for other substrates besides nitroarenes. Essential properties as the structure, coordination, and oxidation state of Cu in these CuNPs are still uncharacterized. Additionally, transfer hydrogenation reaction mechanisms by AB catalyzed by metal nanoparticles have not been investigated so far. Indeed, despite the large interest in these reactions,[25, 32, 33, 61] the mechanisms proposed in the literature are in most part speculative.[42-44, 53, 54, 61, 62]

Here, we fill this knowledge gap by assessing the different reaction mechanisms proposed in the literature for AB-based transfer hydrogenation on copper nanoparticles.[42, 43, 62] We used the hydrogenation of styrene to ethylbenzene as a model reaction, and copper nanoparticles synthetized *in situ* by the reduction of SION-X by AB. The reaction was completed in 2 h at ambient conditions with a >99% selectivity and using water or methanol as the solvent, or their mixtures (see Scheme 1). A combination of gas chromatography-mass spectrometry (GC), X-ray absorption spectroscopy (XAS), NMR, UV-Visible spectroscopy, isotope labeling, and Kohn-Sham density functional methods, were exploited to characterize the reaction products and determine the coordination, and oxidation state of Cu in the NPs, and how they change along the reaction. Isotope labeling and Kohn-Sham density functional methods were exploited to unravel the reaction mechanisms for both AB dehydrogenation and olefin hydrogenation. The key role of the protic solvent in AB dehydrogenation,[32, 33, 42, 62] hypothesized in previous studies, is here experimentally validated. Additionally, we show that the N–H and B–H bonds can follow different dehydrogenation pathways. This study lays the basis for understanding the mechanisms of ammonia borane dehydrogenation on metal nanoparticles.

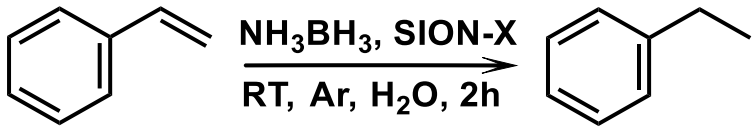

Scheme 1. Styrene hydrogenation reaction on CuNPs.

2. MATERIALS AND METOHODS

A detailed description of the experimental and computational methods used is reported in the Supporting Information.

3. RESULTS AND DISCUSSION

Structure and Reactivity of CuNPs. SION-X was synthetized following the procedure reported in Kinik at al.[54] and doubling the amount of reagents used. Bulk structural properties were confirmed by X-ray powder diffraction (XRPD), infrared spectroscopy (FTIR), and UV-Vis spectroscopy (see Figure S1). The UV-Vis spectrum of SION-X (red curve in Figure 1b and Figure S1f) is very similar to the spectrum of $Cu(OH)_2$ (black curve in Figure S1f), as expected considering the similarity of the Cu oxidation state and coordination environment in the two materials. The absorption peak in the UV region near 360 nm can be assigned to the ligand to metal charge transfer (LMCT), while the broad band in the visible region near 650 nm is due to the Cu(II) *d-d* transition.[63] The absorption peak at 251 nm looming over the 360 nm signal is associated to surface plasmon absorption, based on the literature of copper oxide nanoparticles.[64]

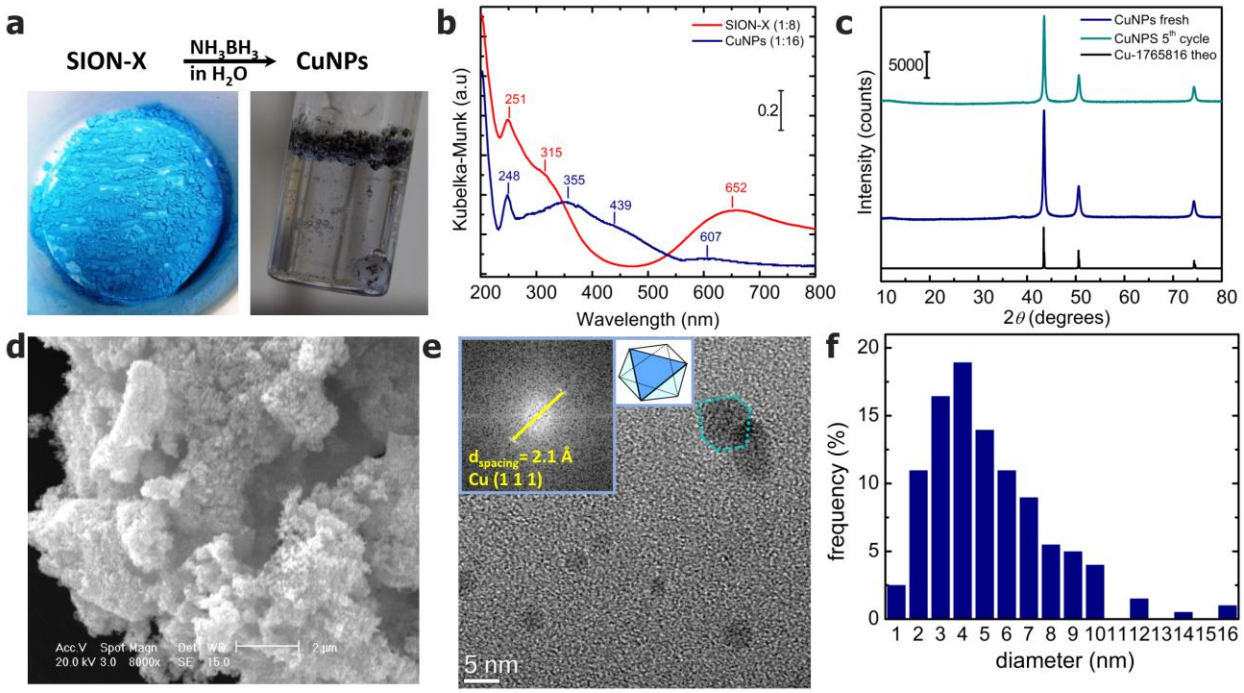

Figure 1. Characterization of CuNPs. a. Reaction scheme for the synthesis of the CuNPs. **b.** DR-UV-Vis spectra of SION-X (red line) and CuNPs (blue line) in the air. The sample powders have been diluted in $BaSO_4$ (sample:$BaSO_4$ weight ratios are reported in parentheses on the plot). **c.** XRPD patterns of CuNPs, as obtained from the reaction of SION-X and AB (blue) and after the 5^{th} cycle of the hydrogenation reaction (light blue) followed by filtration and drying. Patterns collected in the air. The powder pattern simulated for bulk Cu is also shown for comparison (black line). **d.** SEM image of CuNPs. **e.** HRTEM image of CuNPs. The diffraction pattern obtained by Fast Fourier transform of the region highlighted in blue is reported in the inset. A possible scheme of the origin of the hexagonal projection commonly observed for these CuNPs is also shown in an inset. **f.** Histogram of CuNPs size distribution as obtained from HRTEM measurements.

Copper nanoparticles were obtained from SION-X using the same reaction conditions used in the styrene hydrogenation experiments (Figure 1a). XRPD (blue line, Figure 1c) and DR-UV-Vis spectroscopy (blue line, Figure 1b) confirmed that the formed black aggregates are metal copper nanoparticles. In particular, the DR-UV-Vis spectrum of the CuNPs in powder (dry) form shows similar features as those reported by Henglein for CuNPs in solution, with absorption at 248, 355, 439, and 607 nm.[65] These signals can be associated to surface plasmon resonance in copper nanoparticles.[65-70] All the signals are broad and featureless absorbance bands, as expected based on the literature, for nanoparticles having a dimension lower than 4 nm.[65, 69-71] The band at 600 nm can be alternatively assigned to Cu(I) species,[72] although their presence can be excluded based on the XAS measurements (see below). Optical bands of metal nanoparticles are known to be significantly affected by the dielectric constant of the medium.[68] The spectrum of the CuNPs recorded in water is reported in Figure 2a and Figure S5a (dark blue line). In this case, the spectrum is almost featureless, with only a residual band at 190 nm. SEM image in Figure 1d shows nanoparticles as fluffy aggregates of the order of μm, SEM resolution limits the detail on the structure to about 100 nm. To appreciate the shape and dimension of the nanoparticles, they have been characterized using HRTEM. The CuNPs show both spherical and polyhedric shapes, as highlighted from the detailed HRTEM characterization of a single nanoparticle (Figure 1f), whose Fast Fourier Transform (FFT) reveals a lattice fringe of 2.1 Å which corresponds to the (111) plane. Accordingly, (111) planes are responsible of the most intense peak in the CuNPs XRPD pattern (see Figure 1c). Most part of the polydredric particles show an hexagonal projection in the HRTEM images (nanoparticle outlined with a blue line in Figure 1f, see also Figure S3b), that can be associated to different type polyhedra (e.g., octahedra as in the inset of Figure 1f). The few nanometers size of the CuNPs suggested by UV-Vis measurements is confirmed by three

independent techniques: HRTEM, XAS, and XRPD. The size distribution obtained by HRTEM is shown in Figure 1f. It indicates a monodisperse distribution of the particle size, 1 – 16 nm, with a maximum around 4 nm. Calvin et al.[73] have shown that the size of nanoparticles derived from XRPD and XAS can be considered the upper and lower bound of the size distribution, respectively. CuNP size estimated from XRPD data in Figure 1c, using the Sherrer equation, is comprised between 14 and 23 nm (18±4 nm on average), i.e. very close to the largest value in the size distribution obtained by HRTEM (16 nm). XAS indicates that the smallest particles have a dimension of 1.6 nm, i.e. very close to the lowest value in the size distribution obtained by HRTEM shown in Figure 1f: 1 nm (see Table S1).

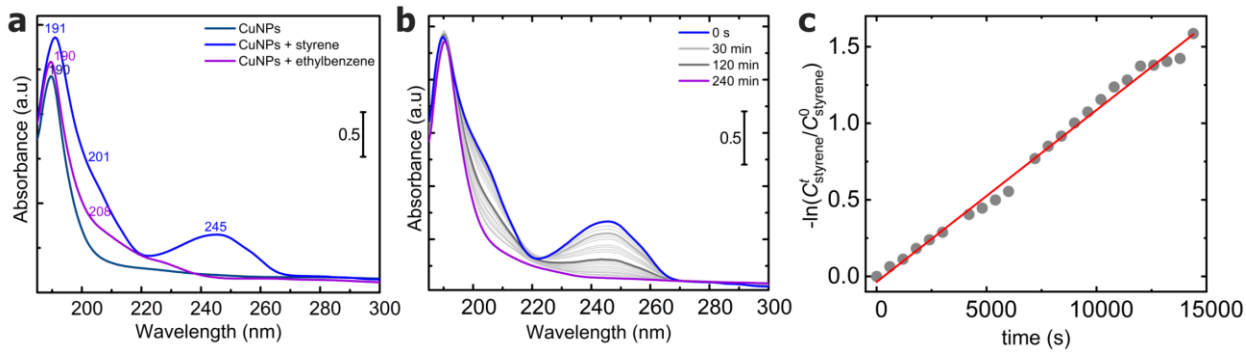

Figure 2. UV-Vis spectra of styrene hydrogenation catalyzed by CuNPs in operando. a. Spectra of aqueous solution of CuNPs before (dark blue line) and after addition of styrene (light blue line) or ethylbenzene (violet line). **b.** Spectra recorded in time of the transfer hydrogenation of AB to styrene catalyzed by CuNPs (RT, air). A lower concentration of reagents was used in the UV measurements than in the catalytic tests to keep the absorbance in the linear range of the detector. The reaction was monitored through the decrease in intensity of the 245 nm band of styrene (see also Figure S8). **c.** Kinetic plot showing $-\ln\left(C^t_{\text{styrene}}/C^{t=0}_{\text{styrene}}\right)$ as function of the

reaction time (grey circle), where C^{t}_{styrene} is the concentration of styrene at the time *t*. The linear fit is reported as a red line (r^2 = 0.99).

The catalytic activity of the CuNPs obtained from the reduction of SION-X was successfully tested for the hydrogenation of olefins using the styrene to ethylbenzene model reaction (see Table 1).[74] In a typical experiment, AB and styrene were added to an aqueous suspension of SION-X kept under inert atmosphere. At ambient conditions, we did not observe the conversion of styrene in absence of a catalyst (entry 8, Table 1), in agreement with previous works.[75]

Table 1. Transfer hydrogenation of styrene to ethylbenzene by ammonia borane catalyzed by *in situ* generated CuNPs.[a]

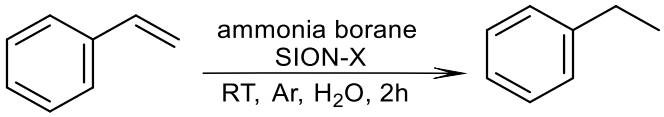

Entry	**SION-X (mmol)**	**NH_3BH_3 (mmol)**	**Solvent**	**Conversion (%)[b]**
1	0.025	0.25	H_2O	100
2	0.025	0.17	H_2O	62
3	0.025	0.25	CH_3OH	100
4	0.025	1.5	H_2O	100

5	0.025	1.5	THF	0
6	0.0025	1.5	H_2O	100
7	0.0025	0.25	H_2O	5
8	–	1.5	H_2O[c]	0

[a] 0.5 mmol of styrene, 5 mL of solvent. [b] Analyzed by GC-MS. [c] Reaction times of 2 h and 18 h.

Supposing the full release of 3 H_2 from each ammonia borane complex, the stoichiometric amount of AB (moles, n_{ABmin}) corresponds to:

$$n_{\mathrm{ABmin}} = \frac{1}{3}(n_{\mathrm{styrene}} + 2n_{\mathrm{SION-X}})$$

where n_{styrene} and $2n_{\mathrm{SION-X}}$ are the moles of styrene and SION-X, respectively. Two moles of AB per mole of SION-X are necessary in order to reduce the two Cu(II) present in the formula unit of SION-X to Cu(0). Aiming at minimizing the amount of SION-X and AB used in the reaction, different SION-X:AB:styrene ratios were tested.[54] The most relevant results are reported in Table 1. For what concerns aprotic solvents (THF), styrene was not hydrogenated even using a large excess of AB (10 times n_{ABmin}, entry 5). Considering protic solvents, complete conversion of styrene was achieved using even a slight excess of AB (entries 1, 3, and 6 in Table 1). It is important to notice that this amount of AB is > 6-fold smaller than the one employed in previous studies on transfer hydrogenation reactions catalyzed by CuNPs to other substrates.[42, 43, 54] Efforts to use exactly the minimum theoretical values brought to only partial conversion of styrene (see entry 2), suggesting that a portion of H_2 (~30%) is lost in the gas phase. This is likely associated

to faster kinetics for AB dehydrogenation than for styrene hydrogenation, as confirmed by DFT calculations (see below).

Recycle experiments were performed by using CuNPs preformed from the reaction of SION-X and AB. In each cycle, the CuNPs were filtered out from the solution, washed with water, acetone, and again water in the air, and then added to an aqueous solution of AB and styrene. The water was treated with ultrasound in Ar to remove the dissolved oxygen before adding AB and styrene. The reaction was stopped after 1 h and the styrene conversion was quantified using GC-MS. We adopted a shorter time in the recycling study than the one used for the catalytic tests (1 h vs. 2 h) to obtain only a partial conversion of styrene (~45%). This was done because a reaction time corresponding only to a partial conversion of styrene allows to evidence more easily changes in the catalytic activity in cycling tests.[76] The CuNPs showed no significant changes in product yield or selectivity after 5 cycles, with conversions ranging from 42 to 46% (see Figure 3). This result is particularly significant, demonstrating the stability and the sustainability of the process.

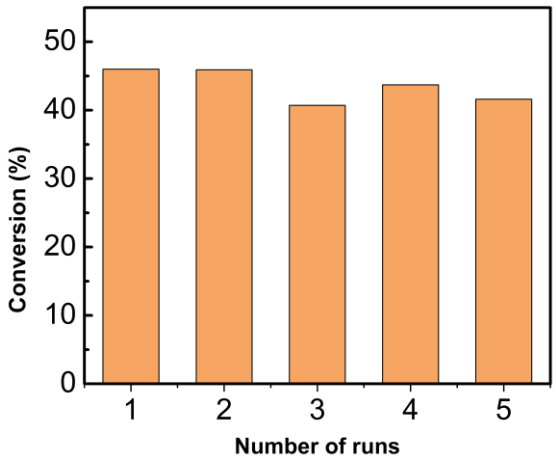

Figure 3. Cycling of CuNPs as catalyst for the transfer hydrogenation of AB to styrene. Conditions: 0.5 mmol of styrene, 5 mL of H_2O, 0.025 mmol CuNPs, 1.5 mmol NH_3BH_3, RT, 1 h.

The oxidation state of copper was monitored using *in situ* XAS spectroscopy (see Figure 4) and operando UV-Vis spectroscopy (see Figure 2b and Figure S7). *In situ* X-ray absorption spectroscopy provided evidence of changes in the oxidation state and coordination of Cu in SION-X after reduction following the reaction with AB and styrene (see Figure 4). Near edge absorption spectroscopy (XANES) is sensitive to the geometry and coordination of the absorption site (Cu). The XANES spectra of SION-X before and after reaction with AB and styrene, or with styrene only, are shown in Figure 4a. The spectra of the pristine SION-X and that after reaction with styrene only are identical, indicating that no reaction occurs in the absence of AB. When AB is introduced, the spectra match that of the CuNPs reference, confirming the formation of CuNPs both in anoxic (SION-X+styrene+AB, Figure 4a) and oxic conditions (SION-X+sytrene+AB_O_2, Figure 4a). The oxic conditions were obtained by short exposure of the solution to the air to test the stability of CuNPs to oxidation. Linear combination fitting of the XANES spectra of SION-X, SION-X+styrene, and SION-X+styrene+AB (oxic and anoxic) with the reference spectra of $Cu(OH)_2$, $CuSO_4$, CuH, CuO, and CuO_2 (Figure S10), indicates that none of these species is present before or after the reaction of SION-X with styrene+AB or styrene only, at least in amounts > 5 – 10% wt., which is the detection limit of this procedure.[77] The position of the absorption edge confirms that Cu is in the 2+ oxidation state in SION-X and SION-X+styrene and in the 0 oxidation state in SION-X+styrene+AB (oxic and anoxic) (Figures S9 and S10). Previous XPS measurements showed, along a majority of Cu(0) species, also the presence of Cu(I) and Cu(II) species.[54] Nevertheless, the presence of Cu(I) and Cu(II) was associated by Kinik et al.[54] to the surface oxidation of CuNPs due to the exposure of the sample to air during the sample preparation for XPS. The extended part of the absorption spectra (EXAFS) is informative of the local structure

around Cu (bond lengths and coordination numbers). The Fourier transform of the extended part of the EXAFS signals extracted from the absorption spectra is shown in Figure 4b. The peaks correspond to the distances from the Cu atom. In SION-X and SION-X+styrene, the Cu-O (1.95±3 Å) and Cu-Cu (2.94±3 Å) distances and coordination numbers (respectively 4 and 2) are compatible with the structure of Jacquesdietrichite[60] within the experimental error, while in the SION-X+styrene+AB (oxic and anoxic) the Cu-Cu distance (2.55±3 Å) matches that of the CuNPs and bulk metallic Cu references (Table S1). The refined first shell coordination number of SION-X+styrene+AB (anoxic) is reduced with respect to the bulk metallic Cu value (12) and is similar to that of the CuNPs reference (9±1, Table S1), confirming the nanoparticulate nature of the reaction product. The first shell coordination number of SION-X+styrene+AB-O_2 (oxic) is further reduced to 7±1 (Table S1), indicating a smaller size of the NPs with respect to its anoxic counterpart (see Section S6 and Table S1 for further details). This means that short exposure to the air can be used as a simple way to decrease (slightly) CuNPs dimensions. Short exposure to the air does not cause a decrease in the catalytic activity of the CuNPs or a change of Cu oxidation state, likely because of the negative standard oxidation potential of copper and to the ability of AB to act as reducing agent of the copper, besides as hydrogen source for the transfer hydrogenation reaction.

The reduction of the coordination number can be used to estimate the size of the nanoparticle. Following the method reported in Calvin et al.,[73] we obtained a CuNP size of 1.6 nm for SION-X+styrene+AB and 0.8 nm for SION-X+styrene+AB-O_2 (Table S1). These values are compatible with the particle size distribution size observed at the TEM (1 – 16 nm, with the majority of them measuring 4 nm: see Figure 1f), as the NP size calculated from XAS must be considered as a lower bound.[73] On the other hand, the NP size estimated from XRPD data, using the Sherrer equation,

was comprised between 14 and 23 nm (18±4 on average, depending which reflection peak was used to calculate it). However, according to Ref. [73], XRPD values should be considered as an upper bound.

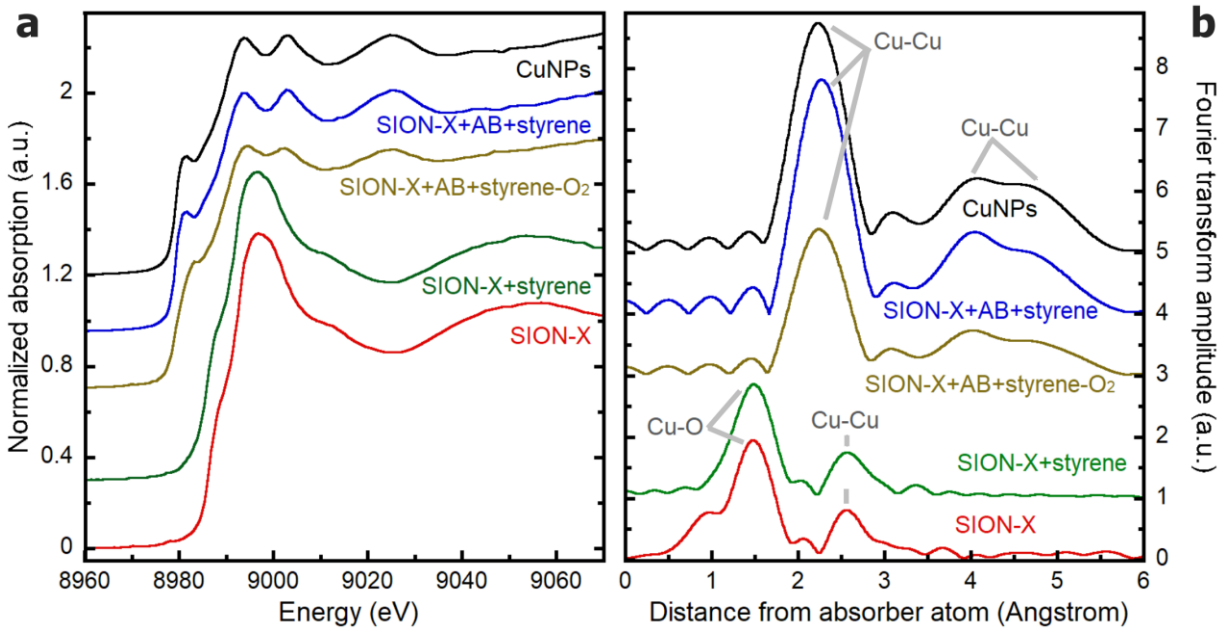

Figure 4. In situ Cu K-edge XAS measurements. a. XANES spectra of aqueous solution of SION-X (2mM, red curve), SION-X + styrene (SION-X: 2mM, styrene: 40mM, green curve), SION-X + AB + styrene after 30 minutes reaction time in anoxic conditions (SION-X: 2mM, styrene: 40mM, AB: 120mM, blue curve), and SION-X + AB + styrene after 120 minutes reaction time in oxic conditions (brown curve). The spectrum of CuNPs obtained from the reaction of 25 mg of $CuSO_4 \cdot 5\ H_2O$ with 12 mg $NaBH_4$ in 2.5 mL of water is also reported for comparison (black curve). The spectra were vertically shifted for easy of view. **b.** Fourier transform of the EXAFS signals extracted from the XAS spectra in panel **a** showing the local structure around Cu. The peaks corresponding to the main contributions to the EXAFS signal arising from the Cu-O or Cu-Cu interactions are labeled on the plot. The distance is not correct for the phase shift. The corrected distances are reported in Table S1. The color legend is the same as panel **a**.

Operando UV-Vis spectroscopy (see Figure 2b and Figure S7) provided similar results to XAS spectroscopy concerning the Cu oxidation state. No formation of bands associated with the formation of Cu(II) or Cu(III) species was observed over the whole reaction time. The formation of Cu(I) species cannot be excluded, having Cu(I) no *d-d* transition and being then not easily detectable with this spectroscopy. However, *in situ* XAS spectra did not reveal Cu(I) compounds, at least at concentrations > 5–10 wt. (Figure 4). Additionally, UV-Vis spectroscopy allows to follow the styrene conversion in time, having styrene a characteristic band at 245 nm[78] that is absent in ethylbenzene (see Figures S4-S6). This band decreases in intensity constantly over two hours of reaction, as result of styrene consumption (see Figure 2b, Figure S7, and Figure S8). By assuming a first order kinetic, it is possible to verify the linear trend of $-\ln\left(C^{t}_{\text{styrene}}/C^{t=0}_{\text{styrene}}\right)$ versus the reaction time (Figure 2c). This allowed to calculate the apparent kinetic constant *k*, being $k = 1.12 \cdot 10^{-4}\ s^{-1}$.

Mechanism of Ethylbenzene Formation. We sought to identify and validate the reaction mechanism(s) proposed in the literature[42, 62] for the transfer hydrogenation of AB to organic substrates catalyzed by the CuNPs, using the styrene to ethylbenzene as a model reaction.

Vasilikogiannaki et al.[62] proposed a plausible two-step mechanism for the transfer hydrogenation of alkynes by AB on gold nanoparticles, where only the B–H bond inserts into gold.[79] This mechanism is indicated as **Ntrans** mechanism in the following and it is shown in Figure 5c. The key role of a protic solvent ROH to allow the full dehydrogenation of AB was also explained in Ref. [62] through the mechanism in Figure 5b, i.e. following the same process reported for metal-catalyzed AB hydrolysis or alcoholysis.[55] Kusy and Grela[42] proved that the mechanisms shown in

Figure 5b and c for gold nanoparticles are also reasonable for CuNPs. In particular, the diphenylacetylene hydrogenation by NH_3BH_3 in THF–D_2O resulted in the formation of 81% of the partial deuterated product, as expected from the mechanism in Figure 5b where the solvent hydrogenates only the N moiety.[42]

Copper nanoparticles can catalyze hydrogenation reactions using H_2 as the hydrogen source.[38-40] Using a reactor, we have verified that these CuNPs catalyze the styrene hydrogenation reaction at ambient temperature using 10 bar H_2. This means that a mechanism, where the hydrogenation of the substrate is mediated by the surface, is also possible for these CuNPs (indicated as **surftrans** mechanism in Figure 5a).

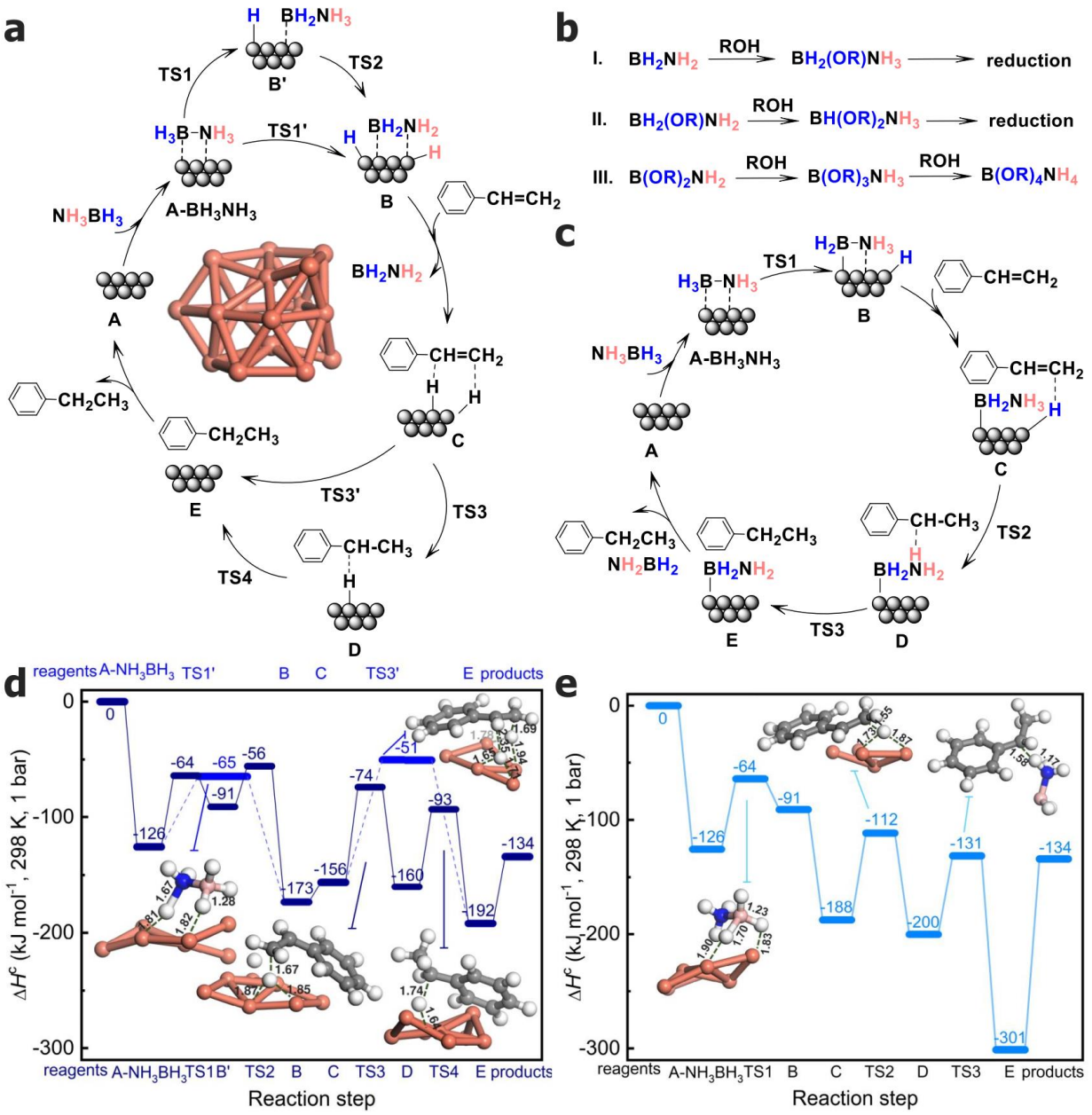

Figure 5. Mechanisms of transfer hydrogenation by ammonia borane to styrene on CuNPs. Two mechanisms were considered in the computational study: **a.** the ammonia borane dehydrogenates on the copper nanoparticles with the formation of BH_2NH_2 and then the hydrogen transfer to the alkene double bond is delegated to the copper surface (**surftrans** mechanism); **c.** only the B–H bond dehydrogenates on the copper surface, while the amino directly transfers the

hydrogen to the benzylic carbon (**Ntrans** mechanism). The formed BH_2NH_2 can re-enter the hydrogenation cycles in place of NH_3BH_3 after reacting with a protic solvent ROH (water or methanol in the present study) forming $(RO)H_2BNH_3$, as suggested by Vasilikogiannaki et al.[62] and Kusy and Grela.[42] The process can be reiterated until the formation of $B(OR)_2NH_2$, as summarized in part **b**. In part **a**, the structure of the cluster used to model the Cu nanoparticles (**A** intermediate) is reported, as optimized at the M06-L/def2-TZVP level. Color code: orange (copper). **d.** Computational reaction profile of transfer hydrogenation by ammonia borane to styrene on CuNPs through the **surftrans** mechanism (part **a**). The dark blue line follows the central cycle in part **a** while the light blue line corresponds to the alternative pathways. **e.** Computational reaction profile of transfer hydrogenation by ammonia borane to styrene on CuNPs through the **Ntrans** mechanism (see part **b**). The optimized structures are shown for selected transition states. Color code: grey (carbon), white (hydrogen), pink (boron), blue (nitrogen), orange (copper). Data obtained at the M06-L/def2-TZVP level using the Cu_{16} cluster reported in part **a**.

We have then considered the mechanisms reported in Figure 5a and b with the aim to test and validate them using both experimental and DFT calculations. For what concerns the mechanism in Figure 5b, previously validated in Refs. [42, 62], it was also confirmed here by the test in THF, reported as entry 5 in Table 1 (see above).

The low polarity of Cu–H species and the almost zero-energy bond dissociation of surface hydrogen species on copper surface previously highlighted in the literature[80, 81] is here confirmed by using TEMPO (2,2,6,6-tetramethyl-1-piperidinyloxy) as a free radical scavenger. For these tests, D_2O/MeOD (1:1) was used as the solvent. TEMPO suppresses the hydrogenation reaction:

only a small amount of ethylbenzene was observed after two hours of reaction for TEMPO to styrene ratio of 1:4, while 100% was formed in absence of TEMPO. GC-MS analysis evidenced the formation of TEMPOH (m/z = 157.21) and TEMPOD (m/z = 158.21), i.e., the addition products of H· or D· to TEMPO· (see spectra in Figure S37). The presence of TEMPOH/D in the reaction mixture was also confirmed by ^{13}C NMR spectroscopy (see Section S9). These results indicate a radical-like nature of the Cu–H/Cu–D species.

Isotope labeling experiments have been exploited to test the **Ntrans** (Figure 5c) and **surftrans** mechanisms (Figure 5a). Three different deuterated forms of AB have been used: ND_3BH_3, NH_3BD_3, and ND_3BD_3. Although several attempts, ND_3BD_3 was not obtained in a pure deuterated form on the N moiety and it contained a significant impurity of THF (see Section S7): therefore, the results for ND_3BD_3 are not discussed in the following (see Section S8.3 for these results). N–H and N–D moieties undergo to a fast isotope exchange with –OD and –OH species, respectively. Protonic (H_2O) and deuterated (CD_3OD/D_2O) solvents have been then used in combination with NH_3BD_3 and ND_3BH_3, respectively, to maintain the isotopic composition of AB unaltered along the reaction. The reaction products have been analyzed using ^1H (see Figures S20 and S26), ^2H (see Figures S21 and S27), and ^{13}C NMR (see Figure 6b and c, Figures S23-S25, and Figure S29) spectroscopy. The results were also validated using GC-MS.

The **surftrans** pathway does not allow to discriminate the origin of the H/D being the transfer hydrogenation surface-mediated: using ND_3BH_3 or NH_3BD_3 would bring indifferently to a stochastic distribution of all the four deuterated forms of ethylbenzene (Ph–CH_2–CH_3, Ph–CH_2–CH_2D, Ph–CHD–CH_3, and Ph–CHD–CH_2D; Ph = phenyl). The **Ntrans** mechanism instead should bring to different isotopic forms of ethylbenzene depending on the use of ND_3BH_3 or NH_3BD_3 as hydrogen source. **Ntrans** consists of two steps: the transfer of an H/D from the B moiety to the

CuNP surface (**A-BH_3-NH_3 → B** step in Figure 5c) and the direct transfer of the H/D from the N moiety (**D → E** step). Using ND_3BH_3, the only expected product should be Ph–CHD–CH_3 if "pure" **Ntrans** is the only mechanism at play for the transfer hydrogenation, while Ph–CH_2–CH_2D will be obtained via NH_3BD_3. Nevertheless, based on the experiment using H_2 gas, we are aware that the CuNPs surface can directly hydrogenate the double bond. This means that a secondary pathway can stem from step **B** of the **Ntrans** mechanism, where a H couple originating from two different B moieties could hydrogenate the unsaturated carbon bond following a surface-mediated mechanism, identical to steps **C → E** in **surftrans** (**surfB** mechanism). The experimental observation that NMe_3BH_3 shows 26% conversion of phenylacetylene in presence of CuNPs would support the presence of this side mechanism of **Ntrans**.[42] The presence of this secondary pathway should bring to the additional formation of Ph–CH_2–CH_3 using ND_3BH_3, and of Ph–CHD–CH_2D for NH_3BD_3.

Using computational methods, we have also investigated an alternative mechanism where the N–H bond in AB is cleaved first, in a preliminary part of this study. Any optimized structure for the $[H\cdots NH_2BH_3]^{\dagger}$ transition state (for both the gas phase or considering the reaction mediated by the copper surface) showed the contribution from a dissociating B–H bond. Additionally, the optimized structure of $BH_3NH_2\cdot$ corresponds to BH_2NH_2 in interaction with a H·. This means that the dissociation of AB cannot start from the N–H moiety and if additional products are observed, they can derive only from **surftrans** mechanism. An experimental confirmation of this computational results can be found in the work conducted by Kusy and Grela[42] reporting that 0% conversion of diphenylacetylene was obtained using NH_3BPh_3 as the hydrogen source, i.e. a molecule that can dehydrogenate only from the N moiety.

A summary of the results obtained by NMR for the isotope labeling experiments is shown in Figure 6a. ^{1}H and ^{2}H NMR results agree and confirm the ^{13}C NMR ones: for the sake of brevity, ^{1}H and ^{2}H NMR spectra and their interpretation are then reported in the Supplementary Information (Section S8). ^{13}C NMR spectrum of the reaction using ND_3BH_3 in CD_3OD/D_2O is reported in Figure 6b. The ^{13}C NMR spectrum is composed by two singlets at 29.58 and 16.10 ppm, that are attributed to $–CH_2$ and $–CH_3$ groups of $Ph–CH_2–CH_3$, respectively. Two additional signals are present: (i) a 1:1:1 triplet centered at 29.23 ppm ($^{1}J_{13C\text{-}D}$ = 19.40 Hz) and (ii) a singlet at 16.04 ppm. They are assigned to–CHD and $–CH_3$ of $Ph–CHD–CH_3$, respectively. No signals associated with $Ph–CH_2–CH_2D$ and $Ph–CHD–CH_2D$ can be detected. This rules out the **surftrans** mechanism and indicates that both the **Ntrans** and **surfB** mechanisms are active using ND_3BH_3. The signals associated with $Ph–CHD–CH_3$ and $Ph–CH_2–CH_3$ are sufficiently separated in the ^{13}C NMR spectra (secondary isotope shifts $^{1}\Delta\delta_{13C}$ and $^{2}\Delta\delta_{13C}$ of 0.35 and 0.08 ppm, respectively, with $^{n}\Delta\delta_{13C} = \delta_{13C/D} – \delta_{13C/H}$) allowing to quantify their relative ratio of the two isotopes to 2:1.

As mentioned above, NH_3BH_3 in deuterated protic solvents undergoes a fast N–H/N–D exchange. Previous studies on the hydrogenation of alkynes using NH_3BH_3 in deuterated protic solvents (D_2O,[42] CD_3OD,[62] or $THF–D_2O$)[62] showed that products having two C–D on the same double bond did not form, while the semi-deuterated (60% for p-methoxyphenylacetylene[62] and 81% for diphenylacetylene)[42] and the not-deuterated products were observed. These results on alkynes agree with what obtained here for olefins: only the **Ntrans** (and **surfB**) pathway is active for ND_3BH_3, while the **surftrans** pathway is suppressed.

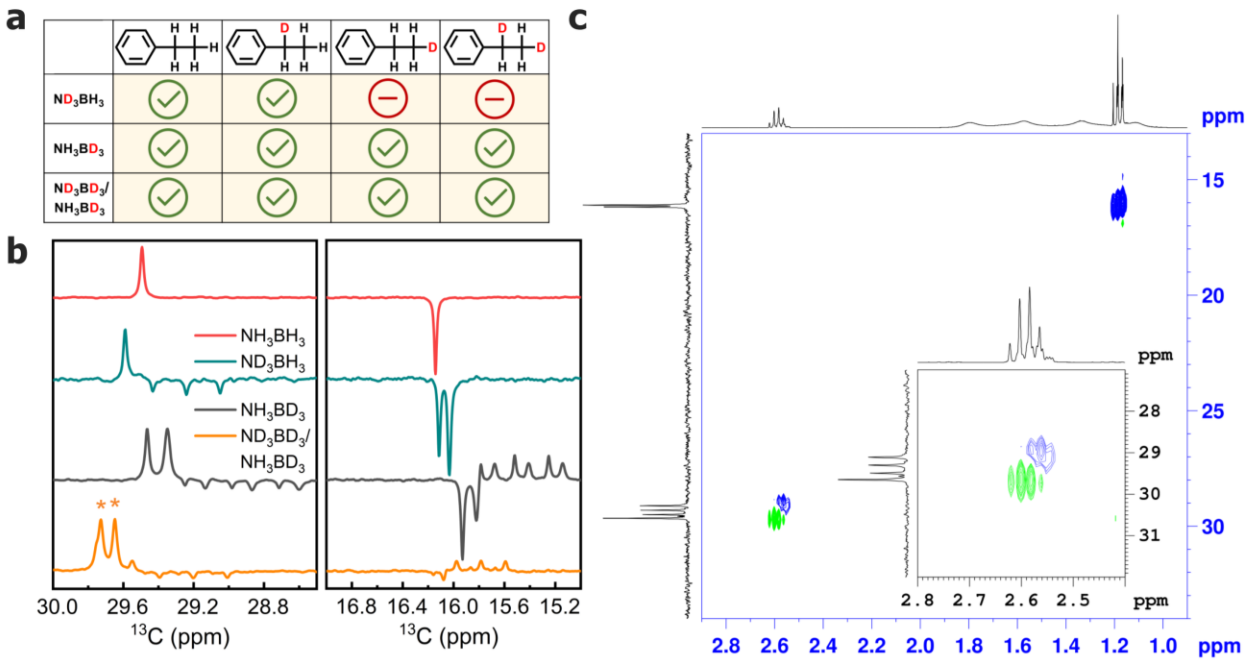

Figure 6. Isotope labeling of ammonia borane. a. The isotopes of ethylbenzene as obtained as reaction products of the transfer hydrogenation of styrene by using different AB isotopes are reported. **b**. ^{13}C NMR spectra, normalized to the highest peak in the 30-28 ppm region. The asterisks mark the signals associated with THF impurities. **c.** 2D-HSQC sensitive improved NMR spectra of hydrogenation reaction of styrene with ND_3BH_3 recorded in CD_3OD:D_2O (5:1) (–CH and $–CH_3$, blue; $–CH_2$, green).

The **Ntrans** and **surfB** mechanisms using NH_3BD_3 should bring to the exclusive formation of Ph–CH_2–CH_2D and Ph–CHD–CH_2D, respectively. Instead, in this case the ^{13}C spectrum of the reaction products showed the presence of all the four isotopes of ethylbenzene (see Figure 6a and Figure S29): Ph–CH_2–CH_3 (peaks at 29.40 ppm and 15.99 ppm), Ph–CHD–CH_3 (singlet centered at 15.89 ppm, and a 1:1:1 triplet centered at 28.96 ppm with $^1J_{13C\text{-}D}$ = 19.40 Hz), Ph-CH_2-CH_2D (singlet at 29.23 ppm, and 1:1:1 triplet at 15.67 ppm with $^1J_{13C\text{-}D}$ = 19.50 Hz), and Ph-CHD-CH_2D

(1:1:1 triplet centered at 28.88 ppm with $^{1}J_{13C\text{-}D}$ = 19.40 Hz, and 1:1:1 triplet centered at 15.59 ppm with $^{1}J_{13C\text{-}D}$ = 19.50 Hz). The formation of Ph–CH_2–CH_3 and Ph–CHD–CH_3 indicates that the reaction follows also the **surftrans** pathway.

Isotope labeling indicate that deuteration of the N moiety suppresses the **surftrans** pathway. Nevertheless, the **surftrans** pathway (and likely also **Ntrans** and **surfB**) is undoubtedly active if the N moiety is hydrogenated. We have used DFT functionals methods to obtain a quantification of the energetics at play along the reaction pathways to help the interpretation of the isotope labeling experiments. The reaction profiles obtained for the **surftrans** and the **Ntrans** mechanisms are reported in part d and e of Figure 5, respectively. The reaction profile for **surfB** can be obtained by merging the **A** → **B** step in **Ntrans** with the **C** → **E** steps in **surftrans**. The considerations made in the following for **surftrans** and the **Ntrans** can be then easily extended to **surfB**.

The cluster model used here undergoes structural reconfiguration as the reaction proceeds. This contribution to the total energy can affect the energetics of the reaction more than in the real nanoparticles because of the smaller size of the model (0.7 vs. 4 nm). Thus, the energies corresponding to the structure change of the cluster have been quantified for each step of both the **surftrans** and the **Ntrans** pathways, verifying that they affect the activation enthalpies by ≤12% (see Tables S4 and S5).

Both **surftrans** and the **Ntrans** mechanisms consider as first step the adsorption of NH_3BH_3 on a CuNP (**A** → **A-NH_3BH_3**). The adsorption is exothermic by –125.6 kJ mol^{-1}. The interaction with the copper surface occurs through the BH_3 moiety, while it was not possible to optimize **A-NH_3BH_3** with AB interacting through the ammonia with the more external atoms of the nanoparticle. The adsorption of NH_3BH_3 is followed by the cleavage of the B–H bond, with the

formation of BH_2NH_3 (directly bonded to a Cu atom) and an H atom (**A-NH_3BH_3 → B** in **Ntrans** and **A-NH_3BH_3 → B'** in **surftrans**) through the transition state **TS1**. This reaction step is endothermic (+35 kJ mol^{-1}), with a computed activation enthalpy (ΔH^{c}_{TS1}) is of 62 kJ mol^{-1}. The H atom in **B**/**B'** is not directly bonded to a single Cu atom, but it is shared among different Cu atoms with the shorter Cu–H distance of 1.78 Å.

The **surftrans** pathway proceeds with the breaking of the N–H bond (**B' → B**), bringing to the formation of NH_2BH_2 (directly bonded to a Cu atom) and of a second H atom. The reaction is strongly exothermic (–82 kJ mol^{-1}), with an activation enthalpy of +35 kJ mol^{-1} i.e., 27 kJ mol^{-1} lower than ΔH^{c}_{TS1}. The competitive mechanism to the two-step AB dehydrogenation just described is the single-step one (**A-NH_3BH_3 → B** step in **surftrans**). This single-step reaction is exothermic by –47 kJ mol^{-1} and it has an activation enthalpy coinciding with ΔH^{c}_{TS1} (63 kJ mol^{-1}). The computed activation enthalpies for AB dehydrogenation well compare with the experimental activation energies reported for Cu-based catalysts (36-52 kJ mol^{-1})[82] and they are compatible with the observed catalytic activity of CuNPs for AB dehydrogenation at RT. The Cu–H bond length is about 1.78-1.83 Å (considering different locations on the Cu cluster) and each H atom is in general shared between two Cu atoms. The Hirshfield charge on the Cu and H is +0.04-0.05 and –0.15 a.u., respectively. All these values support the low strength of the Cu–H bond and the radical-like nature of the hydrogen atoms, that can be described as free surface species.

After the formation of the hydride species, in the **surftrans** mechanism, boranamine is displaced (ΔH^{c}_{des} = 130 kJ mol^{-1}) by styrene (ΔH^{c}_{ads} = –113 kJ mol^{-1}, **C-surftrans**) from the copper surface. It is important to stress that the **B → C** step in **surftrans** is not necessary in the real system because of the larger surface of the nanoparticles than the model used here. Because boranamine acts as a

spectator to the styrene hydrogenation reaction, we do not expect that this extra step (**B → C**) used in the model significantly affects the computed energetics. Boranamine has to be released in the solution at a certain point also in the real catalyst to participate to the reactions described in Figure 5b: this is necessary for ammonia borane to release more than 2 H, as verified experimentally. Styrene can then undergo to a single- (blue curve in Figure 5d) or a two-step (dark blue curve) hydrogenation from the H atoms adsorbed on the copper surface. The two-step hydrogenation involves the hydrogenation of the methylidene group (**C → D**, through the transition state **TS3**) followed by the hydrogenation of the benzylic carbon (**D → E**, **TS4**), while in the single-step both the carbons are hydrogenated at the same time (**C → E** step through the transition state **TS3'** in Figure 5a). The calculations indicate that the single-step hydrogenation although exothermic ($\Delta H^{c}_{C \rightarrow E}$ = –36 kJ mol^{-1}), has a too high transition state enthalpy to be kinetically relevant at ambient conditions ($\Delta H^{c}_{TS3\prime-surftrans}$ = 105 kJ mol^{-1}). For the two-step reaction, both steps are exothermic and characterized by lower activation enthalpies than the single-step process: 82 ($\Delta H^{c}_{TS3-surftrans}$) and 67 kJ mol^{-1} ($\Delta H^{c}_{TS4-surftrans}$), respectively, with the hydrogenation of the methylidene group representing the rate determining step.

For the **Ntrans** mechanism, we have considered a two-step hydrogenation of styrene too. The hydrogenation of the methylidene group (**C → D**) is mediated by the copper surface as in **surftrans**. Unlike **surftrans**, the hydrogenation of the benzylic carbon (**D → E**) is instead obtained by the direct transfer of the hydrogen from the N moiety of –BH_2NH_3. Both these steps are exothermic by –12 ($\Delta H^{c}_{C \rightarrow D}$, see Figure 5e) and –101 kJ mol^{-1} ($\Delta H^{c}_{D \rightarrow E}$). Their activation enthalpies are +76 ($\Delta H^{c}_{TS2-Ntrans}$) and +69 kJ mol^{-1} ($\Delta H^{c}_{TS2-Ntrans}$), respectively. Comparing the activation enthalpies in Figure 5e, it is evident that the hydrogenation of the methylidene group represents the rate determining step also in **Ntrans**. The activation enthalpy is lower in **Ntrans**

than in **surftrans** by 6 kJ mol^{-1}, a difference that is important at ambient temperature, making the **Ntrans** mechanism kinetically favored over the **surftrans**. The structure of the transition states in the two mechanisms (**TS2-Ntrans** and **TS3-surftrans**) is identical, differing only by the presence/absence of $–BH_2NH_3$ on the copper nanoparticle in **Ntrans**/**surftrans**, respectively. For what concerns the hydrogenation of the benzylic carbon, the **Ntrans** mechanism is decidedly favored over the **surftrans** on the thermodynamic point of view: the reaction enthalpy is in fact of –101 kJ mol^{-1} for **Ntrans** to be compared with –32 kJ mol^{-1} for **surftrans**. This extrastabilization is associated with the contemporaneous formation of BH_2NH_2 from the $–BH_2NH_3$ radical, absent in the analogous step in **surftrans**.

These calculations indicate that the **Ntrans** is kinetically and thermodynamically favored over the **surftrans** (and **surfB**), although the similarity of the activation enthalpy associated with the determining step in the two mechanisms (the hydrogenation of the methylidene group, surface-mediated for both the mechanisms) would imply that **surftrans** should be also present, although less favored with respect to **Ntrans**. The NH_3BD_3/H_2O experiment indicates in fact the coexistence of both mechanisms. The suppression of **surftrans** in the ND_3BH_3/CD_3OD-D_2O reaction should be then associated with a modification of the relative ΔH_{TS}^{c} due to the isotopic substitution on the nitrogen.

To shed light on this point, we have then evaluated how the activation enthalpy associated with the **A-NH_3BH_3 → B-surftrans** and **B'-surftrans → B-surftrans** reaction steps are affected by the isotopic substitution on the N moiety. These two steps represent the main difference between **surftrans** and **Ntrans** because they allow the hydrogen atom transfer from N–H to the copper surface. The computed activation enthalpies for ND_3BH_3 are larger than those calculated for NH_3BH_3. For NH_3BH_3, the cleavage of one B–H bond (**A-NH_3BH_3 → B'-surftrans** and **A-**

NH_3BH_3 → B-Ntrans) has the same activation barrier of the contemporaneous B–H and N–H bond dissociation (**A-NH_3BH_3 → B-surftrans**), being of 62 and 63 kJ mol^{-1}, respectively. For ND_3BH_3, $\Delta H^{c}_{TS1\prime-surftrans}$ increases to 68 kJ mol^{-1}, making **A-ND_3BH_3 → B-surftrans** less kinetically favored with respect to **A-ND_3BH_3 → B'-surftrans**. Additionally, the $\Delta H^{c}_{TS2-surftrans}$ for the transfer of the hydrogen atom from N–D to the copper surface (**B'-surftrans → B-surftrans**) is of 41 kJ mol^{-1}, 6 kJ mol^{-1} higher than for N–H. These results indicate that, while for N–H the transfer of the hydrogen atom to the copper surface has the same activation enthalpy of the transfer from B–H (i.e. the first step in **Ntrans** and **surftrans** are happening at the same rate), for N–D the activation barrier is 6 kJ mol^{-1} higher. This corresponds to a 17% increase in the $\Delta H^{c}_{TS2-surftrans}$ activation enthalpy and to a 11-fold decrease in the equilibrium constant. This means that ND_3BH_3 dehydrogenate faster on the B moiety than on the N moiety, i.e. the dehydrogenation by the copper surface stops at $-BH_2ND_3$, and do not proceed to BH_2ND_2, favoring on the kinetic point of view **Ntrans** over **surftrans**. This analysis is corroborated by the fact that **surfB** product was always observed in combination with **Ntrans**, although it coincides with **surftrans** for the hydrogenation of styrene. These results explain why using ND_3BH_3 we do observe only the products associated with **Ntrans** and **surfB**. For NH_3BD_3, deuteration affects both **Ntrans/surfB** and **surftrans**, being the hydrogen transfer from B–H/B–D to the copper surface common to both mechanisms. Because NH_3BD_3 isotope labeling is not favoring one mechanism over the other, products from **Ntrans**, **surfB**, and **surftrans** mechanisms have been observed due to the similarities of the activation and reaction enthalpies of the pathways. The effect of N–H substitution with N–D is negligible on the activation barrier for its inner-sphere addition mechanism to the substrate, i.e. the **D-Ntrans → E-Ntrans** reaction: $\Delta H^{c}_{TS3-surftrans}$ goes from 69 to 72 kJ mol^{-1}, respectively.

4. CONCLUSIONS

In situ generated CuNPs from SION-X can affect the transfer hydrogenation by AB of olefins, in particular the hydrogenation of styrene to ethylbenzene. No reversibility of the reaction or coke formation was observed. The stability of the catalyst was verified over five reaction cycles, even exposing it to the air between two consecutive cycles. This peculiarity over other metal nanoparticles is associated to the negative standard oxidation potential of copper and to the ability of AB to act as reducing agent of the copper and as hydrogen source for the transfer hydrogenation reaction. We confirmed the key role of the protic solvent in guaranteeing the full release of the 3 moles of H_2 per mole of NH_3BH_3, already verified in previous studies for other reactions. The reaction was completed in a few hours by using H_2 gas at 10 bar. Using a combination of isotopic labeling experiments and DFT calculations, we assessed two mechanisms: **Ntrans**, where the transfer of the hydrogen from the NH_3 moiety to the substrate happens through an inner-sphere addition mechanism and **surftrans**, a double surface-mediated hydrogen transfer mechanism. The results indicated that both the **Ntrans** and **surftrans** mechanisms are kinetically relevant in the transfer hydrogenation of NH_3BH_3 on copper nanoparticles. A significant kinetic isotope effect was observed by deuterating the ammonia, which increases the activation enthalpy associated with the N–D scission by the copper surface, suppressing *de facto* the **surftrans** mechanism. These results shed light on the complex mechanisms behind transfer hydrogenation reactions using ammonia borane as hydrogen source and metal nanoparticles as the catalysts. The identification of the reaction paths and the transition states' structure here reported is expected to benefit this important area of research, allowing the design of more efficient catalysts for transfer hydrogenation reactions[22, 40, 83] and of new systems for liquid state hydrogen storage.[84]

ASSOCIATED CONTENT

AUTHOR INFORMATION

Corresponding Author

*E-mail: jg.vitillo@gmail.com

Funding Sources

This research was funded by the Royal Society of Chemistry through the RSC Research Fund grant under Award No. R21-5866640195.

Supporting Information.

The following files are available free of charge.

Detailed descriptions experimental and computational methods, including of synthesis protocols, materials characterization, reactivity experiments, and DFT calculations with supplementary results (PDF)

Cartesian coordinates of computational models (ZIP)

ACKNOWLEDGMENT

This work was supported by the Royal Society of Chemistry through the RSC Research Fund grant under Award No. R21-5866640195. The authors are grateful to the ESRF for providing beamtime (CH-6251) and to Dr. Francesco D'Acapito for assistance during the XAS measurements at the ESRF BM8 — LISA beamline. Flaminia Gianchiglia is acknowledged for the help during the beamtime at ESRF. Gabriele Carugati is acknowledged for the SEM measurements. The authors acknowledge the Minnesota Supercomputing Institute (MSI) at the University of Minnesota for providing computational resources.

ABBREVIATIONS

CuNPs, copper nanoparticles; XAS, X-ray Absorption Spectroscopy; KS-DFT, Kohn-Sham Density Functional Theory.

REFERENCES

1. Blaser, H.-U.; Spindler, F.; Thommen, M., Industrial Applications. In *The Handbook of Homogeneous Hydrogenation*, de Vries, J. G.; Elsevier, C. J., Eds. WILEY-VCH Verlag GmbH & Co. KGaA: Weinheim, 2006; pp 1279-1324.
2. Puprasit, K.; Wongsawaeng, D.; Ngaosuwan, K.; Kiatkittipong, W.; Assabumrungrat, S., Improved hydrogenation process for margarine production with no trans fatty acid formation by non-thermal plasma with needle-in-tube configuration. *J. Food Eng.* **2022,** *334*, 111167.
3. Saudan, L. A., Hydrogenation Processes in the Synthesis of Perfumery Ingredients. *Acc. Chem. Res.* **2007,** *40* (12), 1309-1319.
4. Zhan, X.; Zhu, H.; Ma, H.; Hu, X.; Xie, Y.; Guo, D.; Chen, M.; Ma, P.; Sun, L.; Wang, W. D., et al., Ultrafine PdCo bimetallic nanoclusters confined in N-doped porous carbon for the efficient semi-hydrogenation of alkynes. *Dalton Trans.* **2022,** *51* (42), 16361-16370.
5. Zhang, F.-H.; Zhang, F.-J.; Li, M.-L.; Xie, J.-H.; Zhou, Q.-L., Enantioselective hydrogenation of dialkyl ketones. *Nat. Catal.* **2020,** *3* (8), 621-627.
6. Bekaert, J.; Petrov, M.; Aperis, A.; Oppeneer, P. M.; Milošević, M. V., Hydrogen-Induced High-Temperature Superconductivity in Two-Dimensional Materials: The Example of Hydrogenated Monolayer MgB2. *Phys. Rev. Lett.* **2019,** *123* (7), 077001.
7. Adu-Mensah, D.; Mei, D.; Zuo, L.; Zhang, Q.; Wang, J., A review on partial hydrogenation of biodiesel and its influence on fuel properties. *Fuel* **2019,** *251*, 660-668.
8. Chen, B.; Dingerdissen, U.; Krauter, J. G. E.; Lansink Rotgerink, H. G. J.; Möbus, K.; Ostgard, D. J.; Panster, P.; Riermeier, T. H.; Seebald, S.; Tacke, T., et al., New developments in hydrogenation catalysis particularly in synthesis of fine and intermediate chemicals. *Appl. Catal. A* **2005,** *280* (1), 17-46.
9. Sukjit, E.; Tongroon, M.; Chollacoop, N.; Yoshimura, Y.; Poapongsakorn, P.; Lapuerta, M.; Dearn, K. D., Improvement of the tribological behaviour of palm biodiesel via partial hydrogenation of unsaturated fatty acid methyl esters. *Wear* **2019,** *426-427*, 813-818.
10. Cao, X.; Zhao, J.; Long, F.; Liu, P.; Jiang, X.; Zhang, X.; Xu, J.; Jiang, J., Efficient low-temperature hydrogenation of fatty acids to fatty alcohols and alkanes on a Ni-Re bimetallic catalyst: The crucial role of NiRe alloys. *Appl. Catal. B* **2022,** *312*, 121437.
11. Bulushev, D. A.; Ross, J. R. H., Vapour phase hydrogenation of olefins by formic acid over a Pd/C catalyst. *Catal. Today* **2011,** *163* (1), 42-46.
12. Yu, P.; Yang, Z.; Gu, Z.; Wong, H.-W., Catalytic reaction coupling of propane dehydrogenation with nitrobenzene hydrogenation over Pt/Al_2O_3. *Catal. Commun.* **2022,** *166*, 106449.
13. Argyle, M. D.; Bartholomew, C. H., Heterogeneous Catalyst Deactivation and Regeneration: A Review. *Catalysts* **2015,** *5* (1), 145-269.
14. An, Z.; Li, J., Recent advances in the catalytic transfer hydrogenation of furfural to furfuryl alcohol over heterogeneous catalysts. *Green Chem.* **2022,** *24* (5), 1780-1808.

15. Chirik, P. J., Iron- and Cobalt-Catalyzed Alkene Hydrogenation: Catalysis with Both Redox-Active and Strong Field Ligands. *Acc. Chem. Res.* **2015,** *48* (6), 1687-1695.
16. Liu, L.; Corma, A., Metal Catalysts for Heterogeneous Catalysis: From Single Atoms to Nanoclusters and Nanoparticles. *Chem. Rev.* **2018,** *118* (10), 4981-5079.
17. Zaera, F., Nanostructured materials for applications in heterogeneous catalysis. *Chem. Soc. Rev.* **2013,** *42* (7), 2746-2762.
18. Scharnagl, F. K.; Hertrich, M. F.; Ferretti, F.; Kreyenschulte, C.; Lund, H.; Jackstell, R.; Beller, M., Hydrogenation of terminal and internal olefins using a biowaste-derived heterogeneous cobalt catalyst. *Science Adv.* **2018,** *4* (9), eaau1248.
19. Ryabchuk, P.; Agostini, G.; Pohl, M.-M.; Lund, H.; Agapova, A.; Junge, H.; Junge, K.; Beller, M., Intermetallic nickel silicide nanocatalyst—A non-noble metal–based general hydrogenation catalyst. *Science Adv.* **2018,** *4* (6), eaat0761.
20. Zhang, J.; Wang, T.; Shi, C.; Pan, L.; Zhang, X.; Peng, C.; Zou, J.-J., Achieving super dispersed metallic nickel nanoparticles over MCM-41 for highly active and stable hydrogenation of olefins and aromatics. *Chem. Eng. J.* **2023,** *470*, 144197.
21. Alonso, F.; Riente, P.; Yus, M., Nickel Nanoparticles in Hydrogen Transfer Reactions. *Acc. Chem. Res.* **2011,** *44* (5), 379-391.
22. Wang, D.; Astruc, D., The Golden Age of Transfer Hydrogenation. *Chem. Rev.* **2015,** *115* (13), 6621-6686.
23. Sakintuna, B.; Lamari-Darkrim, F.; Hirscher, M., Metal hydride materials for solid hydrogen storage: A review. *Int. J. Hydrogen En.* **2007,** *32* (9), 1121-1140.
24. Castilla-Martinez, C. A.; Moury, R.; Demirci, U. B., Amidoboranes and hydrazinidoboranes: State of the art, potential for hydrogen storage, and other prospects. *Int. J. Hydrogen En.* **2020,** *45* (55), 30731-30755.
25. Yüksel Alpaydın, C.; Gülbay, S. K.; Ozgur Colpan, C., A review on the catalysts used for hydrogen production from ammonia borane. *Int. J. Hydrogen En.* **2020,** *45* (5), 3414-3434.
26. Sarkar, K.; Das, K.; Kundu, A.; Adhikari, D.; Maji, B., Phosphine-Free Manganese Catalyst Enables Selective Transfer Hydrogenation of Nitriles to Primary and Secondary Amines Using Ammonia–Borane. *ACS Catal.* **2021,** *11* (5), 2786-2794.
27. Liu, X.; Longwitz, L.; Spiegelberg, B.; Tönjes, J.; Beweries, T.; Werner, T., Erbium-Catalyzed Regioselective Isomerization–Cobalt-Catalyzed Transfer Hydrogenation Sequence for the Synthesis of Anti-Markovnikov Alcohols from Epoxides under Mild Conditions. *ACS Catal.* **2020,** *10* (22), 13659-13667.
28. Chong, C. C.; Rao, B.; Kinjo, R., Metal-Free Catalytic Reduction of α,β-Unsaturated Esters by 1,3,2-Diazaphospholene and Subsequent C–C Coupling with Nitriles. *ACS Catal.* **2017,** *7* (9), 5814-5819.
29. Ganguly, G.; Malakar, T.; Paul, A., Theoretical Studies on the Mechanism of Homogeneous Catalytic Olefin Hydrogenation and Amine–Borane Dehydrogenation by a Versatile Boryl-Ligand-Based Cobalt Catalyst. *ACS Catal.* **2015,** *5* (5), 2754-2769.
30. Stephens, F. H.; Pons, V.; Tom Baker, R., Ammonia–borane: the hydrogen source par excellence? *Dalton Trans.* **2007,** (25), 2613-2626.
31. Faverio, C.; Boselli, M. F.; Medici, F.; Benaglia, M., Ammonia borane as a reducing agent in organic synthesis. *Org. Biomol. Chem.* **2020,** *18* (39), 7789-7813.
32. Mboyi, C. D.; Poinsot, D.; Roger, J.; Fajerwerg, K.; Kahn, M. L.; Hierso, J.-C., The Hydrogen-Storage Challenge: Nanoparticles for Metal-Catalyzed Ammonia Borane Dehydrogenation. *Small* **2021,** *17* (44), 2102759.

33. Wu, H.; Cheng, Y.; Fan, Y.; Lu, X.; Li, L.; Liu, B.; Li, B.; Lu, S., Metal-catalyzed hydrolysis of ammonia borane: Mechanism, catalysts, and challenges. *Int. J. Hydrogen En.* **2020,** *45* (55), 30325-30340.
34. Liu, M.; Zhou, L.; Luo, X.; Wan, C.; Xu, L., Recent Advances in Noble Metal Catalysts for Hydrogen Production from Ammonia Borane. *Catalysts* **2020,** *10* (7), 788.
35. Zahmakiran, M.; Özkar, S., Transition Metal Nanoparticles in Catalysis for the Hydrogen Generation from the Hydrolysis of Ammonia-Borane. *Top Catal.* **2013,** *56* (13), 1171-1183.
36. Zhao, T.-J.; Zhang, Y.-N.; Wang, K.-X.; Su, J.; Wei, X.; Li, X.-H., General transfer hydrogenation by activating ammonia-borane over cobalt nanoparticles. *RSC Adv.* **2015,** *5* (124), 102736-102740.
37. Metin, Ö.; Mazumder, V.; Özkar, S.; Sun, S., Monodisperse Nickel Nanoparticles and Their Catalysis in Hydrolytic Dehydrogenation of Ammonia Borane. *J. Am. Chem. Soc.* **2010,** *132* (5), 1468-1469.
38. Chen, S.; de Souza, P. M.; Ciotonea, C.; Marinova, M.; Dumeignil, F.; Royer, S.; Wojcieszak, R., Micro-/mesopores confined ultrasmall Cu nanoparticles in SBA-15 as a highly efficient and robust catalyst for furfural hydrogenation to furfuryl alcohol. *Appl. Catal. A* **2022,** *633*, 118527.
39. Gawande, M. B.; Goswami, A.; Felpin, F.-X.; Asefa, T.; Huang, X.; Silva, R.; Zou, X.; Zboril, R.; Varma, R. S., Cu and Cu-Based Nanoparticles: Synthesis and Applications in Catalysis. *Chem. Rev.* **2016,** *116* (6), 3722-3811.
40. Ojha, N. K.; Zyryanov, G. V.; Majee, A.; Charushin, V. N.; Chupakhin, O. N.; Santra, S., Copper nanoparticles as inexpensive and efficient catalyst: A valuable contribution in organic synthesis. *Coord. Chem. Rev.* **2017,** *353*, 1-57.
41. Jeong, S.; Lee, S. H.; Jo, Y.; Lee, S. S.; Seo, Y.-H.; Ahn, B. W.; Kim, G.; Jang, G.-E.; Park, J.-U.; Ryu, B.-H., et al., Air-stable, surface-oxide free Cu nanoparticles for highly conductive Cu ink and their application to printed graphene transistors. *J. Mater. Chem. C,* **2013,** *1* (15), 2704-2710.
42. Kusy, R.; Grela, K., Ligand-free (Z)-selective transfer semihydrogenation of alkynes catalyzed by in situ generated oxidizable copper nanoparticles. *Green. Chem.* **2021,** *23* (15), 5494-5502.
43. Park, B. Y.; Lim, T.; Han, M. S., A simple and efficient in situ generated copper nanocatalyst for stereoselective semihydrogenation of alkynes. *Chem. Commun.* **2021,** *57* (56), 6891-6894.
44. Du, J.; Chen, J.; Xia, H.; Zhao, Y.; Wang, F.; Liu, H.; Zhou, W.; Wang, B., Commercially Available CuO Catalyzed Hydrogenation of Nitroarenes Using Ammonia Borane as a Hydrogen Source. *ChemCatChem* **2020,** *12* (9), 2426-2430.
45. Yamada, Y.; Yano, K.; Fukuzumi, S., Catalytic application of shape-controlled Cu2O particles protected by Co3O4 nanoparticles for hydrogen evolution from ammonia borane. *Energy Environ. Sci.* **2012,** *5* (1), 5356-5363.
46. Nowak, A.; Szade, J.; Talik, E.; Ratuszna, A.; Ostafin, M.; Peszke, J., Structural, spectroscopic and biological investigation of copper oxides nanoparticles with various capping agents. *Mater. Chem. Phys.* **2014,** *145* (3), 465-470.
47. Singh, A. K.; Xu, Q., Synergistic Catalysis over Bimetallic Alloy Nanoparticles. *ChemCatChem* **2013,** *5* (3), 652-676.

48. Yao, Y.; Wu, X.; Gutiérrez, O. Y.; Ji, J.; Jin, P.; Wang, S.; Xu, Y.; Zhao, Y.; Wang, S.; Ma, X., et al., Roles of Cu+ and Cu0 sites in liquid-phase hydrogenation of esters on core-shell CuZnx@C catalysts. *Appl. Catal. B* **2020,** *267*, 118698.
49. Liu, H.; Li, X.; Ma, Z.; Sun, M.; Li, M.; Zhang, Z.; Zhang, L.; Tang, Z.; Yao, Y.; Huang, B., et al., Atomically Dispersed Cu Catalyst for Efficient Chemoselective Hydrogenation Reaction. *Nano Lett.* **2021,** *21* (24), 10284-10291.
50. Yu, C.; Fu, J.; Muzzio, M.; Shen, T.; Su, D.; Zhu, J.; Sun, S., CuNi Nanoparticles Assembled on Graphene for Catalytic Methanolysis of Ammonia Borane and Hydrogenation of Nitro/Nitrile Compounds. *Chem. Mater.* **2017,** *29* (3), 1413-1418.
51. Du, J.; Hou, J.; Li, B.; Qin, R.; Xu, C.; Liu, H., Support-free 3D hierarchical nanoporous Cu@Cu_2O for fast tandem ammonia borane dehydrogenation and nitroarenes hydrogenation under mild conditions. *J. Alloys Compd.* **2020,** *815*, 152372.
52. Yun, R.; Zhang, B.; Zhan, F.; Du, L.; Wang, Z.; Zheng, B., Cu Nanoclusters Anchored on the Metal–Organic Framework for the Hydrolysis of Ammonia Borane and the Reduction of Quinolines. *Inorg. Chem.* **2021,** *60* (17), 12906-12911.
53. Kinik, F. P.; Nguyen, T. N.; Oveisi, E.; Valizadeh, B.; Ebrahim, F. M.; Gładysiak, A.; Mensi, M.; Stylianou, K. C., Discovery of a self-healing catalyst for the hydrolytic dehydrogenation of ammonia borane. *J. Mater. Chem. A* **2019,** *7* (41), 23830-23837.
54. Kinik, F. P.; Nguyen, T. N.; Mensi, M.; Ireland, C. P.; Stylianou, K. C.; Smit, B., Sustainable Hydrogenation of Nitroarenes to Anilines with Highly Active in-situ Generated Copper Nanoparticles. *ChemCatChem* **2020,** *12* (10), 2833-2839.
55. Ramachandran, P. V.; Gagare, P. D., Preparation of Ammonia Borane in High Yield and Purity, Methanolysis, and Regeneration. *Inorg. Chem.* **2007,** *46* (19), 7810-7817.
56. Li, H.; Yang, Q.; Chen, X.; Shore, S. G., Ammonia borane, past as prolog. *J. Organomet. Chem.* **2014,** *751*, 60-66.
57. Sutton, A. D.; Burrell, A. K.; Dixon, D. A.; Garner, E. B.; Gordon, J. C.; Nakagawa, T.; Ott, K. C.; Robinson, J. P.; Vasiliu, M., Regeneration of Ammonia Borane Spent Fuel by Direct Reaction with Hydrazine and Liquid Ammonia. *Science* **2011,** *331* (6023), 1426-1429.
58. Yurderi, M.; Bulut, A.; Ertas, İ. E.; Zahmakiran, M.; Kaya, M., Supported copper–copper oxide nanoparticles as active, stable and low-cost catalyst in the methanolysis of ammonia–borane for chemical hydrogen storage. *Appl. Catal., B* **2015,** *165*, 169-175.
59. Hoet, P. H. M.; Brüske-Hohlfeld, I.; Salata, O. V., Nanoparticles – known and unknown health risks. *J. Nanobiotechnol.* **2004,** *2* (1), 12.
60. Kampf, A. R.; Favreau, G., Jacquesdietrichite, $Cu_2[BO(OH)_2](OH)_3$, a new mineral from the Tachgagalt mine, Morocco : Description and crystal structure. *Eur. J. Mineral.* **2004,** *16* (2), 361-366.
61. Zhao, W.; Li, H.; Zhang, H.; Yang, S.; Riisager, A., Ammonia borane-enabled hydrogen transfer processes: Insights into catalytic strategies and mechanisms. *Green Energy Environ.* **2023,** *8* (4), 948-971.
62. Vasilikogiannaki, E.; Titilas, I.; Vassilikogiannakis, G.; Stratakis, M., cis-Semihydrogenation of alkynes with amine borane complexes catalyzed by gold nanoparticles under mild conditions. *Chem. Commun.* **2015,** *51* (12), 2384-2387.
63. Negri, C.; Selleri, T.; Borfecchia, E.; Martini, A.; Lomachenko, K. A.; Janssens, T. V. W.; Cutini, M.; Bordiga, S.; Berlier, G., Structure and Reactivity of Oxygen-Bridged Diamino Dicopper(II) Complexes in Cu-Ion-Exchanged Chabazite Catalyst for NH3-Mediated Selective Catalytic Reduction. *J. Am. Chem. Soc.* **2020,** *142* (37), 15884-15896.

64. Dulta, K.; Koşarsoy Ağçeli, G.; Chauhan, P.; Jasrotia, R.; Chauhan, P. K.; Ighalo, J. O., Multifunctional CuO nanoparticles with enhanced photocatalytic dye degradation and antibacterial activity. *Sustain. Environ. Res.* **2022,** *32* (1), 2.
65. Henglein, A., Formation and Absorption Spectrum of Copper Nanoparticles from the Radiolytic Reduction of Cu(CN)2. *J. Phys. Chem. B* **2000,** *104* (6), 1206-1211.
66. Mallick, K.; Witcomb, M. J.; Scurrell, M. S., In situ synthesis of copper nanoparticles and poly(o-toluidine): A metal–polymer composite material. *Eur. Polym. J.* **2006,** *42* (3), 670-675.
67. Mott, D.; Galkowski, J.; Wang, L.; Luo, J.; Zhong, C.-J., Synthesis of Size-Controlled and Shaped Copper Nanoparticles. *Langmuir* **2007,** *23* (10), 5740-5745.
68. Kelly, K. L.; Coronado, E.; Zhao, L. L.; Schatz, G. C., The Optical Properties of Metal Nanoparticles: The Influence of Size, Shape, and Dielectric Environment. *J. Phys. Chem. B* **2003,** *107* (3), 668-677.
69. Usman, M. S.; Ibrahim, N. A.; Shameli, K.; Zainuddin, N.; Yunus, W. M., Copper Nanoparticles Mediated by Chitosan: Synthesis and Characterization via Chemical Methods. *Molecules* **2012,** *17* (12), 14928-14936.
70. Xiong, J.; Wang, Y.; Xue, Q.; Wu, X., Synthesis of highly stable dispersions of nanosized copper particles using l-ascorbic acid. *Green Chem.* **2011,** *13* (4), 900-904.
71. Peniche, C.; Fernández, M.; Rodríguez, G.; Parra, J.; Jimenez, J.; Bravo, A. L.; Gómez, D.; San Román, J., Cell supports of chitosan/hyaluronic acid and chondroitin sulphate systems. Morphology and biological behaviour. *J. Mater. Sci. Mater. Med.* **2007,** *18* (9), 1719-1726.
72. Bordiga, S.; Pazé, C.; Berlier, G.; Scarano, D.; Spoto, G.; Zecchina, A.; Lamberti, C., Interaction of N2, CO and NO with Cu-exchanged ETS-10: a compared FTIR study with other Cu-zeolites and with dispersed Cu2O. *Catal Today* **2001,** *70* (1), 91-105.
73. Calvin, S.; Miller, M. M.; Goswami, R.; Cheng, S.-F.; Mulvaney, S. P.; Whitman, L. J.; Harris, V. G., Determination of crystallite size in a magnetic nanocomposite using extended x-ray absorption fine structure. *J. Appl. Phys.* **2003,** *94* (1), 778-783.
74. Han, C.; Meng, P.; Waclawik, E. R.; Zhang, C.; Li, X.-H.; Yang, H.; Antonietti, M.; Xu, J., Palladium/Graphitic Carbon Nitride (g-C_3N_4) Stabilized Emulsion Microreactor as a Store for Hydrogen from Ammonia Borane for Use in Alkene Hydrogenation. *Angew. Chem. Int. Ed.* **2018,** *57* (45), 14857-14861.
75. Bakuru, V. R.; Samanta, D.; Maji, T. K.; Kalidindi, S. B., Transfer hydrogenation of alkynes into alkenes by ammonia borane over Pd-MOF catalysts. *Dalton Trans.* **2020,** *49* (16), 5024-5028.
76. Scott, S. L., A Matter of Life(time) and Death. *ACS Catal.* **2018,** *8* (9), 8597-8599.
77. Bardelli, F.; Rimondi, V.; Lattanzi, P.; Rovezzi, M.; Isaure, M.-P.; Giaccherini, A.; Costagliola, P., Pinus nigra bark from a mercury mining district studied with high resolution XANES spectroscopy. *Environ. Sci.: Processes Impacts* **2022,** *24* (10), 1748-1757.
78. Rodebush, W. H.; Feldman, I., Ultraviolet Absorption Spectra of Organic Molecules. III. Mechanical Interference of Substituent Groups with Resonance Configurations. *J. Am. Chem. Soc.* **1946,** *68* (5), 896-899.
79. Fountoulaki, S.; Daikopoulou, V.; Gkizis, P. L.; Tamiolakis, I.; Armatas, G. S.; Lykakis, I. N., Mechanistic Studies of the Reduction of Nitroarenes by $NaBH_4$ or Hydrosilanes Catalyzed by Supported Gold Nanoparticles. *ACS Catal.* **2014,** *4* (10), 3504-3511.
80. Kyriakou, G.; Boucher, M. B.; Jewell, A. D.; Lewis, E. A.; Lawton, T. J.; Baber, A. E.; Tierney, H. L.; Flytzani-Stephanopoulos, M.; Sykes, E. C. H., Isolated Metal Atom Geometries as a Strategy for Selective Heterogeneous Hydrogenations. *Science* **2012,** *335* (6073), 1209-1212.

81. Kristinsdóttir, L.; Skúlason, E., A systematic DFT study of hydrogen diffusion on transition metal surfaces. *Surf. Sci.* **2012,** *606* (17), 1400-1404.
82. Yao, Q.; Lu, Z.-H.; Zhang, Z.; Chen, X.; Lan, Y., One-pot synthesis of core-shell Cu@SiO2 nanospheres and their catalysis for hydrolytic dehydrogenation of ammonia borane and hydrazine borane. *Sci. Rep.* **2014,** *4* (1), 7597.
83. Lau, S.; Gasperini, D.; Webster, R. L., Amine–Boranes as Transfer Hydrogenation and Hydrogenation Reagents: A Mechanistic Perspective. *Angew. Chem. Int. Ed.* **2021,** *60* (26), 14272-14294.
84. Preuster, P.; Papp, C.; Wasserscheid, P., Liquid Organic Hydrogen Carriers (LOHCs): Toward a Hydrogen-free Hydrogen Economy. *Acc. Chem. Res.* **2017,** *50* (1), 74-85.

Table of Contents Graphic